

## SUPPORTING INFORMATION

### Unprecedented bistability domain and interplay between spin crossover and polymorphism in a mononuclear iron(II) complex

Mark B. Bushuev,<sup>\**a,b*</sup> Vasiliy A. Daletsky,<sup>a</sup> Denis P. Pishchur,<sup>a</sup> Yuri V. Gatilov,<sup>c</sup> Ilya V. Korolkov,<sup>a</sup> Elena B. Nikolaenkova<sup>c</sup> and Viktor P. Krivopalov<sup>c</sup>

<sup>a</sup> Nikolaev Institute of Inorganic Chemistry, Siberian Branch of Russian Academy of Sciences, 3, Acad. Lavrentiev Ave., Novosibirsk, Russia. Fax: +7 383 330 94 89; Tel: +7 383 316 51 43; E-mail: bushuev@niic.nsc.ru, mark.bushuev@gmail.com

<sup>b</sup> Novosibirsk State University, 2, Pirogova str., Novosibirsk, Russia.

<sup>c</sup> N. N. Vorozhtsov Novosibirsk Institute of Organic Chemistry, Siberian Branch of Russian Academy of Sciences, 9, Acad. Lavrentiev Ave., Novosibirsk, Russia.

## Table of Contents

### Chemistry

**Synthesis of  $[\text{FeL}_2](\text{BF}_4)_2 \cdot x\text{H}_2\text{O}$ ,  $x \approx 0.5$ , ( $\mathbf{1}^{\text{LS}} \cdot x\text{H}_2\text{O}$ )**

### Crystal Structure Determination

**Crystallographic data of  $[\text{FeL}_2](\text{BF}_4)_2 \cdot x\text{H}_2\text{O}$ ,  $x \approx 0.11$  and  $0.18$**

### X-ray diffraction analysis of polycrystals

### Magnetic measurements

### Thermal analysis

### Thermodynamic properties

**Cooperative effect for the transition  $\mathbf{1}^{\text{A/LS}} \rightarrow \mathbf{1}^{\text{A/HS}}$**

**Table S1** Selected bond lengths (Å) and angles (°) in the crystal structure of

$[\text{FeL}_2](\text{BF}_4)_2 \cdot x\text{H}_2\text{O}$ ,  $x \approx 0.11$

**Fig. S1** Comparison of XRPD pattern of  $\mathbf{1}^{\text{LS}} \cdot x\text{H}_2\text{O}$  (top,  $T = 300$  K) with simulated XPRD pattern (bottom,  $P2_1/n$ ,  $T = 200$  K).

**Fig. S2** TG and DSC curves for the complex  $\mathbf{1}^{\text{LS}} \cdot x\text{H}_2\text{O}$ .

**Fig. S3** Packing of  $\mathbf{1}^{\text{LS}} \cdot x\text{H}_2\text{O}$ .

**Fig. S4** B–F $\cdots$  $\pi$  interactions.

**Fig. S5** C–H $\cdots$ X interactions.

**Fig. S6** C–H $\cdots$  $\pi$  interactions.

**Fig. S7** Thermal variation of  $\chi_M T$  for the spin transition  $\mathbf{1}^{\text{A/LS}} \leftrightarrow \mathbf{1}^{\text{A/HS}}$ .

**Fig. S8** Thermal variation of  $\chi_M T$  for  $\mathbf{1}^{\text{LS}} \cdot x\text{H}_2\text{O}$ .

**Fig. S9** DSC curve for the transition  $\mathbf{1}^{\text{A/LS}} \leftrightarrow \mathbf{1}^{\text{A/HS}}$ .

**Fig. S10** DSC curve for the transformation  $\mathbf{1}^{\text{LS}} \cdot x\text{H}_2\text{O} \rightarrow \mathbf{1}^{\text{B/HS}}$ .

**Fig. S11** DSC curve for the transition  $\mathbf{1}^{\text{B/LS}} \rightarrow \mathbf{1}^{\text{B/HS}}$ .

**Fig. S12** Thermal variation of  $\chi_M T$  for  $\mathbf{1}^{\text{LS}} \cdot x\text{H}_2\text{O}$  (first heating run).

**Fig S13** IR spectra of  $\mathbf{1}^{\text{LS}} \cdot x\text{H}_2\text{O}$ ,  $\mathbf{1}^{\text{A/LS}}$ ,  $\mathbf{1}^{\text{B/LS}}$  and  $\mathbf{1}^{\text{C/LS}}$  ( $3900 - 2600 \text{ cm}^{-1}$ , fluorinated oil).

**Fig S14** IR spectra of  $\mathbf{1}^{\text{LS}} \cdot x\text{H}_2\text{O}$ ,  $\mathbf{1}^{\text{A/LS}}$ ,  $\mathbf{1}^{\text{B/LS}}$  and  $\mathbf{1}^{\text{C/LS}}$  ( $1700 - 350 \text{ cm}^{-1}$ , KBr).

### Sorption/desorption of water in sealed ampoules

**Fig S15** Thermal dependencies of water vapor pressure, saturated water vapor pressure and overall pressure in the ampoule.

## Chemistry

The synthesis was carried out in deoxygenated EtOH under an inert atmosphere of argon. The ligand L was prepared according to the procedure previously reported.<sup>S1</sup> All other reagents and solvents were commercially available and were used without additional purification. Elemental analysis (C, H, N) was performed with a EuroEA3000 analyzer using standard technique. IR absorption spectra were recorded on a Scimitar FTS 2000 spectrometer.

S1 M. B. Bushuev, Y. V. Gatilov, E. B. Nikolaenkova, V. G. Vasiliev and V. P. Krivopalov, *Inorg. Chim. Acta*, 2013, **395**, 95.

### Synthesis of $[\text{FeL}_2](\text{BF}_4)_2 \cdot x\text{H}_2\text{O}$ , $x \approx 0.5$ , ( $\mathbf{1}^{\text{LS}} \cdot x\text{H}_2\text{O}$ )

A solution of L (0.040 mmol, 10.6 mg) in EtOH (1 mL) was added to a stirred solution of  $\text{Fe}(\text{BF}_4)_2 \cdot 6\text{H}_2\text{O}$  (0.020 mmol, 6.8 mg) in EtOH (1 mL). The solution turned dark red. Gentle stirring resulted in the formation of red microcrystalline precipitate. In 45 min the precipitate was filtered off, washed with EtOH, and dried in the ambient air. Yield: 11.5 mg (74%). Dark red precipitate. Elemental analysis (%), calcd for  $\text{C}_{30}\text{H}_{31}\text{N}_{10}\text{B}_2\text{F}_8\text{FeO}_{0.5}$  (769.10): C 46.9, H 4.1, N 18.2,  $\text{H}_2\text{O}$  1.2; found C 47.2, H 4.2, N 18.1,  $\text{H}_2\text{O}$  1.1. IR (KBr): 3625 (w;  $\nu(\text{OH})$ ), 3554 (w;  $\nu(\text{OH})$ ), 3155 (w;  $\nu(\text{CH})$ ), 3121 (w;  $\nu(\text{CH})$ ), 3086 (w;  $\nu(\text{CH})$ ), 2970 (w;  $\nu(\text{CH}_3)$ ), 2928 (w;  $\nu(\text{CH}_3)$ ), 2858 (w;  $\nu(\text{CH}_3)$ ), 1601 (s;  $\nu + \delta(\text{ring})$ ), 1578 (m;  $\nu + \delta(\text{ring})$ ), 1534 (s;  $\nu + \delta(\text{ring})$ ), 1487 (m;  $\nu + \delta(\text{ring})$ ), 1464 (m), 1435 (s), 1400 (s), 1334 (m), 1288 (w), 1242 (w), 1225 (w), 1161 (w), 1055 (s;  $\nu_3(\text{B}-\text{F})$ ), 984 (m), 839 (w), 806 (w), 764 (m), 679 (w), 648 (w), 620 (w), 607 (w), 586 (w), 520 (w;  $\nu_4(\text{B}-\text{F})$ ), 427 (w)  $\text{cm}^{-1}$ . IR (fluorinated oil): 3620 (w;  $\nu(\text{OH})$ ), 3554 (w;  $\nu(\text{OH})$ ), 3120 (w;  $\nu(\text{CH})$ ), 2960 (w;  $\nu(\text{CH}_3)$ ), 2925 (w;  $\nu(\text{CH}_3)$ ), 2853 (w;  $\nu(\text{CH}_3)$ ), 1599 (s;  $\nu + \delta(\text{ring})$ ), 1576 (s;  $\nu + \delta(\text{ring})$ ), 1532 (s;  $\nu + \delta(\text{ring})$ ), 1485 (s;  $\nu + \delta(\text{ring})$ ), 1462 (m), 1435 (s), 1398 (s)  $\text{cm}^{-1}$ . Single crystals were obtained by crystallization from mother liquor.

### Crystal Structure Determination

The data were collected with a red thin needle crystal of  $[\text{FeL}_2](\text{BF}_4)_2 \cdot x\text{H}_2\text{O}$  with a Bruker APEX II CCD diffractometer using graphite monochromated Mo-K $\alpha$  radiation ( $T = 200$  K,  $\lambda = 0.71073 \text{ \AA}$ ). The structure was solved by direct methods and the refinement on  $F^2$  and all further calculations were carried out with the SHELXTL suite.<sup>S2</sup> All non-hydrogen and major

parts of disordered atoms were refined anisotropically. All disordered parts were refined with geometrical restraints. Hydrogen atoms were placed geometrically on their carrier atoms and were refined with a riding model.

S2 G. M. Sheldrick, *Acta Crystallogr., Sect. A* 64, 2008, 112.

### Crystallographic data of $[\text{FeL}_2](\text{BF}_4)_2 \cdot x\text{H}_2\text{O}$ , $x \approx 0.11$ and $0.18$

The crystal was taken directly from the solution and put into the cold stream of dry  $\text{N}_2$  on the goniometer. Formula  $\text{C}_{30}\text{H}_{30.22}\text{B}_2\text{F}_8\text{FeN}_{10}\text{O}_{0.11}$ ,  $M = 761.79$ , monoclinic, space group  $P2_1/n$ ,  $a = 12.035(2)$ ,  $b = 19.525(4)$ ,  $c = 15.481(2)$  Å,  $\beta = 108.03(1)^\circ$ ,  $V = 3459.2(10)$  Å<sup>3</sup>,  $Z = 4$ ,  $D_{\text{calc}} = 1.463$  g·cm<sup>-3</sup>,  $\mu = 0.518$  mm<sup>-1</sup>, crystal size  $0.02 \times 0.03 \times 0.56$  mm, min/max transmission = 0.814/0.988,  $\theta_{\text{max}} = 25.1^\circ$ , measured 19935, unique 6041 ( $R_{\text{int}} = 0.149$ ), observed [ $F_o > 4\sigma(F)$ ] 2643 reflections,  $R_1 = 0.0692$  ( $F_o$ ),  $wR_2 = 0.2104$  (all),  $\text{Gof} = 0.983$ ,  $\Delta\rho_{\text{max}} = 0.45$ ,  $\Delta\rho_{\text{min}} = -0.61$  e·Å<sup>-3</sup>, CCDC 948843. The tetrafluoroborate ions are disordered over two positions with occupancies 0.95:0.05(1) and 0.86:0.14(1). The occupancy of water molecule position is 0.11(1).

The second experiment was made after the crystals had been kept in the ambient air for 4 months. The quality of crystals worsened (mosaicity, *etc.*). We managed to find a crystal and to make an experiment only for  $\theta_{\text{max}} = 20.9^\circ$  at the temperature of 150 K. The structure refinement led to  $R = 0.0895$  (2196  $F_o$ ) and water position occupancy of 0.18(2).

Hydrogen atoms on the lattice water molecule could not be found nor fixed and were omitted from the structural model.

### X-ray diffraction analysis of polycrystals

XPRD analysis of polycrystals was performed on Shimadzu XRD-7000 diffractometer (Cu- $K_\alpha$  radiation, Ni – filter, 5 – 60°  $2\theta$  range, 0.03°  $2\theta$  step, 5s per point). A polycrystalline sample was slightly ground with hexane in an agate mortar, and the resulting suspension was deposited on the polished side of a standard quartz sample holder. A smooth thin layer was formed after drying.

### Magnetic measurements

The study of magnetic properties of the complexes was performed on the Faraday balance in the temperature range 80 – 500 K in the magnetic fields from 5.8 to 10.9 kOe. The

measurements of magnetic susceptibility of the samples showed that it does not depend on the field strength proving the absence of ferromagnetic impurities in the samples. Further measurements of the magnetic susceptibility were performed in the field of 9.09 kOe. The samples were placed into a hermetic quartz ampoule. The molar magnetic susceptibility ( $\chi_M$ ) was calculated taking into account the diamagnetism of the atoms using the Pascal additive scheme.

### Thermal analysis

Simultaneous thermal analysis (STA) of  $\mathbf{1}^{\text{LS}} \cdot x\mathbf{H}_2\mathbf{O}$ , including thermogravimetric (TG) and differential scanning calorimetry (DSC) measurements, was performed with NETZSCH STA 409 PC Luxx (open  $\text{Al}_2\text{O}_3$  crucible, heating rate  $6 \text{ K min}^{-1}$ ,  $60 \text{ ml min}^{-1}$  He flow). Netzsch Proteus Analysis software was used for processing of experimental data.

### Thermodynamic properties

Thermodynamic properties were studied using differential scanning calorimeter NETZSCH DSC 204 F1 Phoenix. DSC measurements of the samples were performed by heat flow measurement method at heating/cooling rate  $6 \text{ K min}^{-1}$  in  $25 \text{ ml min}^{-1}$  Ar flow. The baseline signal obtained by heating two empty crucibles was subtracted from the experimental results for the samples. The sensitivity calibration of the sample carrier sensors and temperature scale graduation included melting peak area measurements of six melting standard samples from calibration set 6.239.2–91.3 supplied by Netzsch. The transition temperatures were defined from the resulting heat flow as intersections of the peak onset with the corresponding baseline. Netzsch Proteus Analysis software was used to determine DSC peak area and transition temperatures and for further averaging the results of 3 experiments.

Thermodynamic properties of  $\mathbf{1}^{\text{A/LS}}$  (after magnetochemical cycling) have been investigated by DSC in a sealed aluminum crucible. Differential scanning measurements were carried out over the temperature range  $293 - 500 \text{ K}$  at warming and cooling modes. Thermal effects associated with the spin transition  $\mathbf{1}^{\text{A/LS}} \leftrightarrow \mathbf{1}^{\text{A/HS}}$  were observed at  $T_{\text{onset}\uparrow} = 483.3 \text{ K}$  (warming mode) and  $T_{\text{onset}\downarrow} = 348.6 \text{ K}$  (cooling mode). Molar enthalpy of transition,  $\Delta H$ , was calculated as the area of the DSC peak. The excess entropy of the transition was calculated by the formula  $\Delta S = \Delta H/T$ , which is valid for the first order phase transitions.

The irreversible transformation of  $\mathbf{1}^{\text{LS}} \cdot x\mathbf{H}_2\mathbf{O}$  into  $\mathbf{1}^{\text{B/HS}}$  and the transition  $\mathbf{1}^{\text{B/LS}} \leftrightarrow \mathbf{1}^{\text{B/HS}}$  were investigated as follows. The first heating run of  $\mathbf{1}^{\text{LS}} \cdot x\mathbf{H}_2\mathbf{O}$  to  $400 \text{ K}$  was performed in an open aluminum crucible. An anomaly at  $T_{\text{onset}\uparrow} = 379.2 \text{ K}$  was accompanied with 1.1 % weight

loss. The second heating of the sample to 500 K was performed in a sealed aluminum crucible. A sharp endo-effect was observed at  $T_{\text{onset}\uparrow} = 464.8$  K. Upon further cycling, only smooth anomalies were observed.

### Cooperative effect for the transition $\mathbf{1}^{\text{A/LS}} \rightarrow \mathbf{1}^{\text{A/HS}}$

The Slichter-Drickamer model (SDM) describes an SCO system in terms of mean field theory as a regular solution of HS and LS molecules. It uses a phenomenological parameter of cooperative interaction,  $\Gamma$ , which reflects the tendency of SCO molecule in a certain spin state to be surrounded by SCO molecules of the same spin state ( $\Gamma > 0$ ). The SDM reproduces various forms of SCO curves as well as hysteresis effect. A first-order phase transition as well as a possibility for hysteretic bistable behavior are predicted when  $\Gamma > 2RT_c$ . The SDM uses the following equation for the HS molar fraction  $\gamma_{\text{HS}}$ :

$$\ln\left(\frac{1-\gamma_{\text{HS}}}{\gamma_{\text{HS}}}\right) = \frac{\Delta H + \Gamma(1-2\gamma_{\text{HS}})}{RT} - \frac{\Delta S}{R}, \quad (1)$$

where  $\Delta H$  and  $\Delta S$  are the enthalpy and entropy changes associated with spin transition.

We calculated the  $\gamma_{\text{HS}}(T)$  values and the value of  $\Gamma$  as follows.

1) Magnetic contributions of HS and LS fractions were extracted from magnetic susceptibility data above and below the transition region.

2) The  $\gamma_{\text{HS}}(T)$  values were calculated at different temperatures from magnetic data using the equation  $\chi'_{\text{M}} = \gamma_{\text{HS}}\chi'_{\text{M}}(\text{HS}) + (1-\gamma_{\text{HS}})\chi'_{\text{M}}(\text{LS})$ , where  $\chi'_{\text{M}}(\text{HS})$  and  $\chi'_{\text{M}}(\text{LS})$  stand for magnetic contributions of HS and LS fractions at high and low temperature limits, respectively.

3) Parameter  $\Gamma$  was determined by the least squares method, by minimizing numerically the sum

$$\sum_T \left[ \ln\left(\frac{1-\gamma_{\text{HS}}(T)}{\gamma_{\text{HS}}(T)}\right) - \frac{\Delta H + \Gamma(1-2\gamma_{\text{HS}}(T))}{RT} + \frac{\Delta S}{R} \right]^2. \quad (2)$$

The Sorai-Seki model (SSM) assumes that the crystal lattice consists of  $N$  non-interacting domains of equal size containing  $n$  molecules and that the spin transition in each domain occurs simultaneously. The SSM does not describe the hysteresis effects. The equation to calculate model value of  $\gamma_{\text{HS}}$  can be written as

$$\gamma_{\text{HS}}^{\text{mod}} = \frac{1}{1 + \exp\left(-\frac{n\Delta H}{R}\left(\frac{1}{T} - \frac{1}{T_{1/2}}\right)\right)}, \quad (3)$$

where  $T_{1/2}$  is the temperature at which the number of domains in the HS and LS forms is equal. The parameter  $n$  was determined by minimizing the sum

$$\sum_T [\gamma_{HS}^{\text{mod}}(T) - \gamma_{HS}(T)]^2. \quad (4)$$

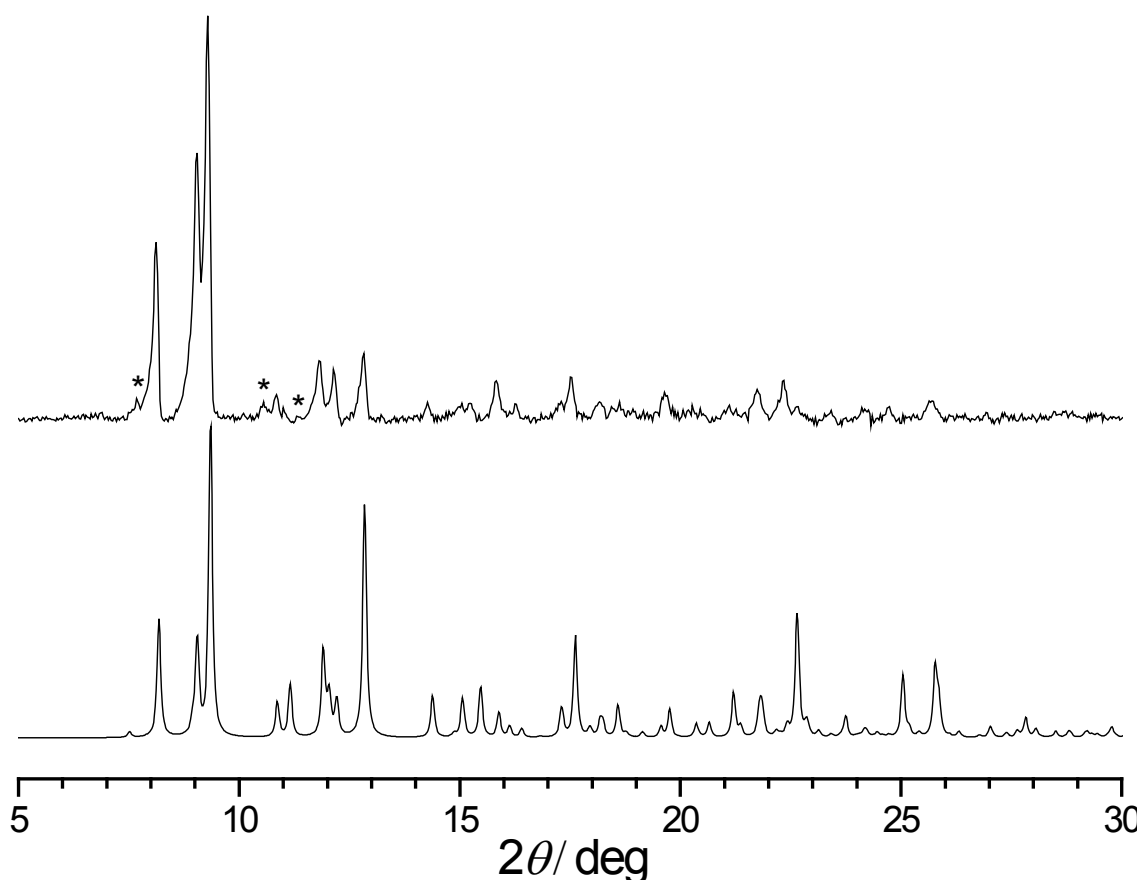
**Table S1**

Selected bond lengths ( $\text{\AA}$ ) and angles ( $^\circ$ ) in the crystal structure of  $[\text{FeL}_2](\text{BF}_4)_2 \cdot x\text{H}_2\text{O}$ ,  $x \approx 0.11$ .

Bond length	
Fe(1)–N(7)	1.870(5)
Fe(1)–N(2)	1.877(5)
Fe(1)–N(10)	1.984(6)
Fe(1)–N(8)	1.987(6)
Fe(1)–N(3)	1.989(5)
Fe(1)–N(5)	1.991(5)

Angle	
N(7)–Fe(1)–N(2)	177.4(2)
N(7)–Fe(1)–N(10)	79.5(2)
N(2)–Fe(1)–N(10)	102.8(2)
N(7)–Fe(1)–N(8)	81.1(2)
N(2)–Fe(1)–N(8)	96.6(2)
N(10)–Fe(1)–N(8)	160.5(2)
N(7)–Fe(1)–N(3)	97.7(2)
N(2)–Fe(1)–N(3)	80.9(2)
N(10)–Fe(1)–N(3)	93.6(2)
N(8)–Fe(1)–N(3)	87.7(2)
N(7)–Fe(1)–N(5)	101.7(2)
N(2)–Fe(1)–N(5)	79.6(2)
N(10)–Fe(1)–N(5)	90.6(2)
N(8)–Fe(1)–N(5)	94.6(2)
N(3)–Fe(1)–N(5)	160.6(2)



**Fig. S1** Comparison of XRPD pattern of  $\mathbf{1}^{\text{LS}} \cdot x\text{H}_2\text{O}$  (top,  $T = 300\text{ K}$ ) with simulated XPRD pattern (bottom,  $P2_1/n$ ,  $T = 200\text{ K}$ ).

The complex shows reasonable agreement between experimental and simulated X-ray powder diffraction (XRPD) pattern. The intensity of unindexed peaks (marked with asterisk) is lower than 5 % of maximum.

Using PowderCell 2.4 programme<sup>S3</sup> we estimated cell parameters of  $\mathbf{1}^{\text{LS}} \cdot x\text{H}_2\text{O}$  at room temperature:  $a = 12.20$ ,  $b = 19.58$ ,  $c = 15.53\text{ \AA}$ ,  $\beta = 108.06^\circ$ . Single crystal data at 200 K are:  $a = 12.035(2)$ ,  $b = 19.525(4)$ ,  $c = 15.481(2)\text{ \AA}$ ,  $\beta = 108.03(1)^\circ$ . Therefore the dependence of cell parameters on temperature is non-isotropic and diffraction pattern will significantly differ at 200 and 300 K.

Differences between calculated and experimental XRPD patterns can also be due to variations in water content in single crystals ( $x = 0.11$ ) and polycrystalline sample ( $x \approx 0.5$ ) which may affect cell parameters.

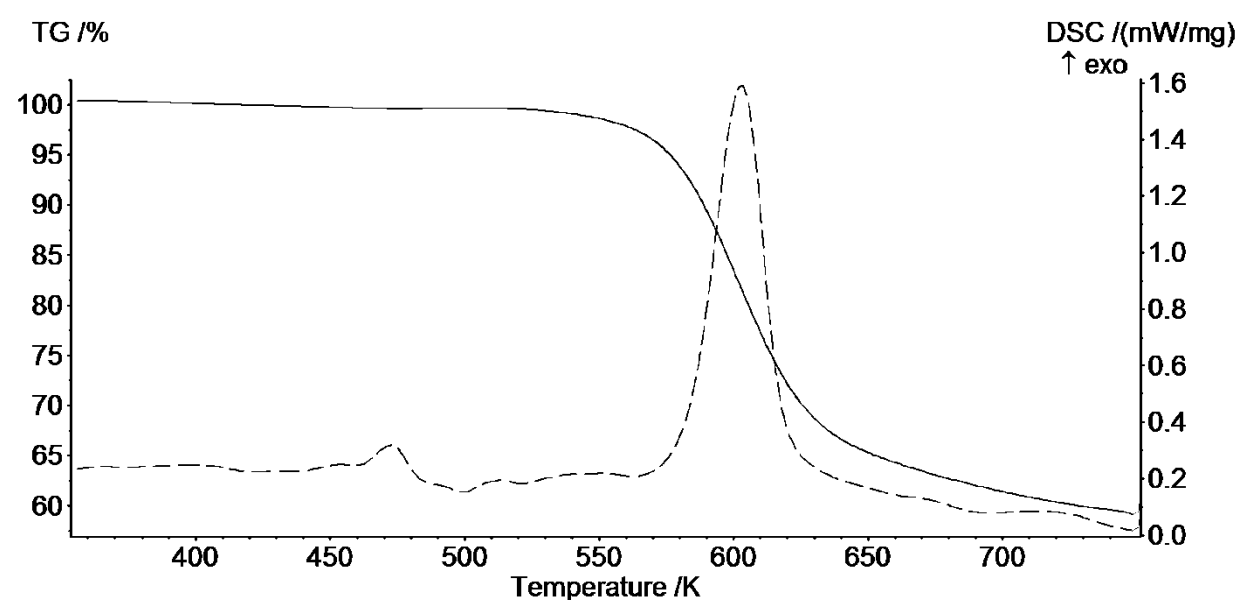


**Fig. S2** TG and DSC curves for the complex  $\mathbf{1}^{\text{LS}} \cdot x\text{H}_2\text{O}$ .

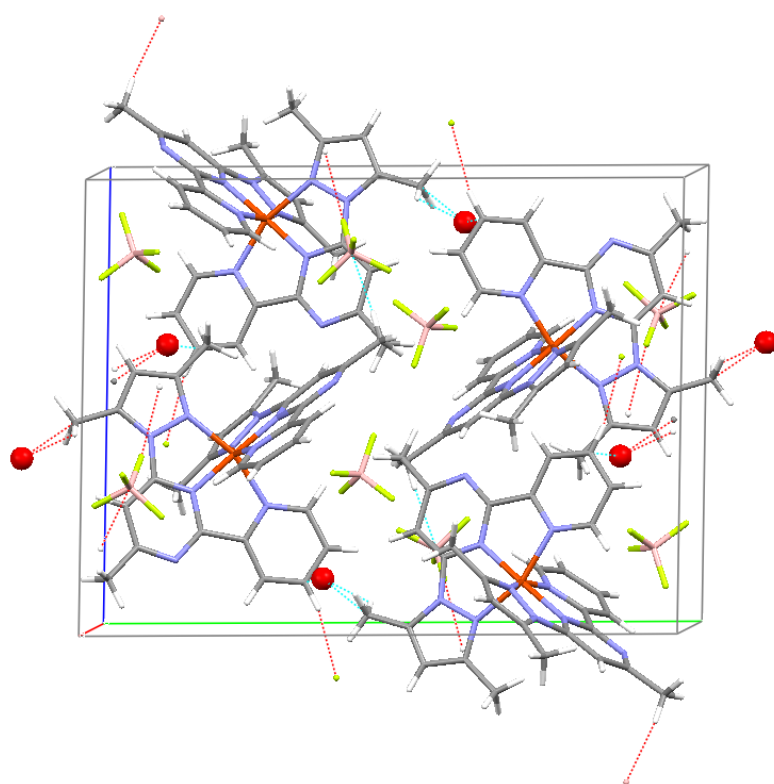


**Fig. S3** Packing of  $\mathbf{1}^{\text{LS}} \cdot x\text{H}_2\text{O}$ . View along  $a$  axis (minor parts of disordered  $\text{BF}_4^-$  are not shown). Short contacts (less than sum of VDW radii by 0.2 Å) are also displayed.

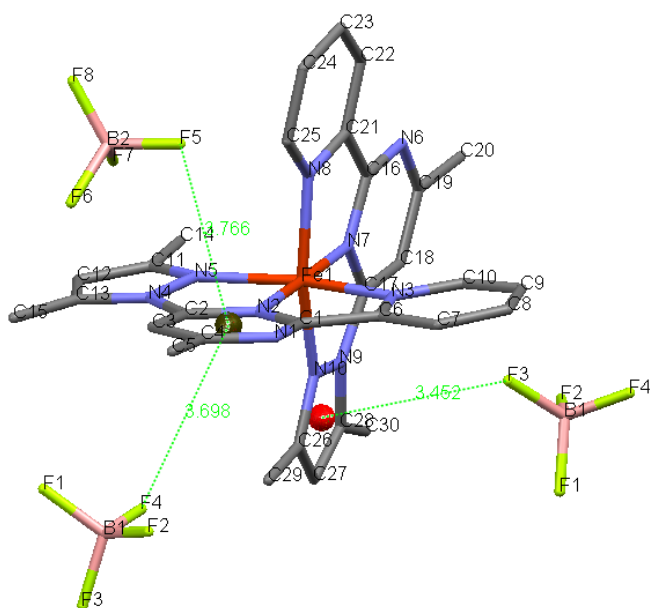


**Fig. S4** B–F...π interactions (minor parts of disordered  $\text{BF}_4^-$  are not shown): B1–F3...centroid (Cg), F3...Cg 3.452(8) Å, B1–F3...Cg 127.5(6)°; B1–F4...Cg, F4...Cg 3.698(7) Å, B1–F4...Cg 116.5(6)°; B2–F5...Cg, F5...Cg 3.765(15) Å, B2–F5...Cg 94.0(8)°.

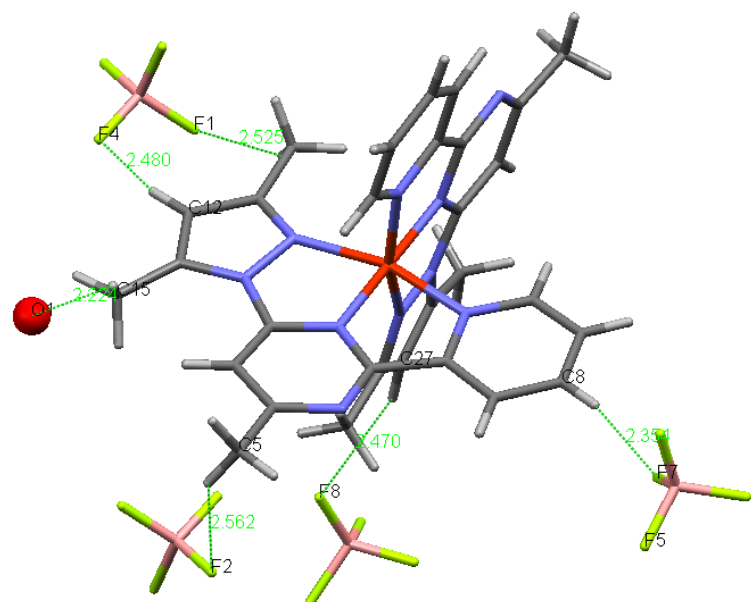


**Fig. S5** C–H $\cdots$ X interactions (minor parts of disordered  $\text{BF}_4^-$  are not shown): C14–H $\cdots$ F1, H $\cdots$ F 2.53 Å, C–H $\cdots$ F 140°; C12–H $\cdots$ F4, H $\cdots$ F 2.48 Å, C–H $\cdots$ F 156°; C5–H $\cdots$ F2, H $\cdots$ F 2.56 Å, C–H $\cdots$ F 139°; C27–H $\cdots$ F8, H $\cdots$ F 2.47 Å, C–H $\cdots$ F 140°; C8–H $\cdots$ F7, H $\cdots$ F 2.35 Å, C–H $\cdots$ F 168°; C15–H $\cdots$ O1, H $\cdots$ O 2.22 Å, C–H $\cdots$ O 130°.

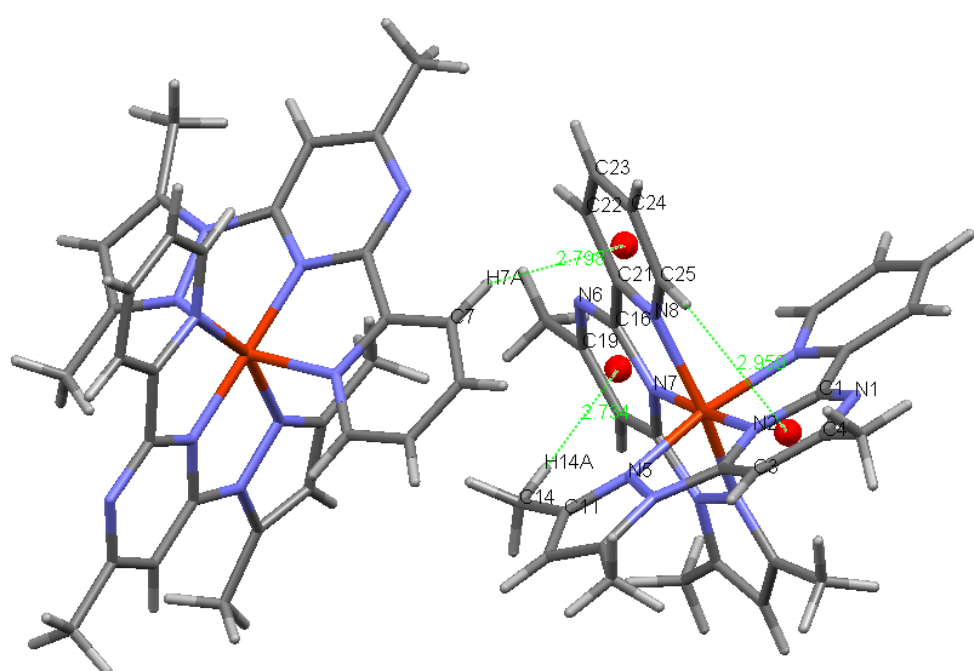


**Fig. S6** C–H $\cdots$  $\pi$  interactions: C7–H $\cdots$ Cg, H $\cdots$ Cg 2.80 Å, C–H $\cdots$ Cg 142°; C14–H $\cdots$ Cg, H $\cdots$ Cg 2.73 Å, C–H $\cdots$ Cg 178°; C25–H $\cdots$ Cg, H $\cdots$ Cg 2.96 Å, C–H $\cdots$ Cg 138°.

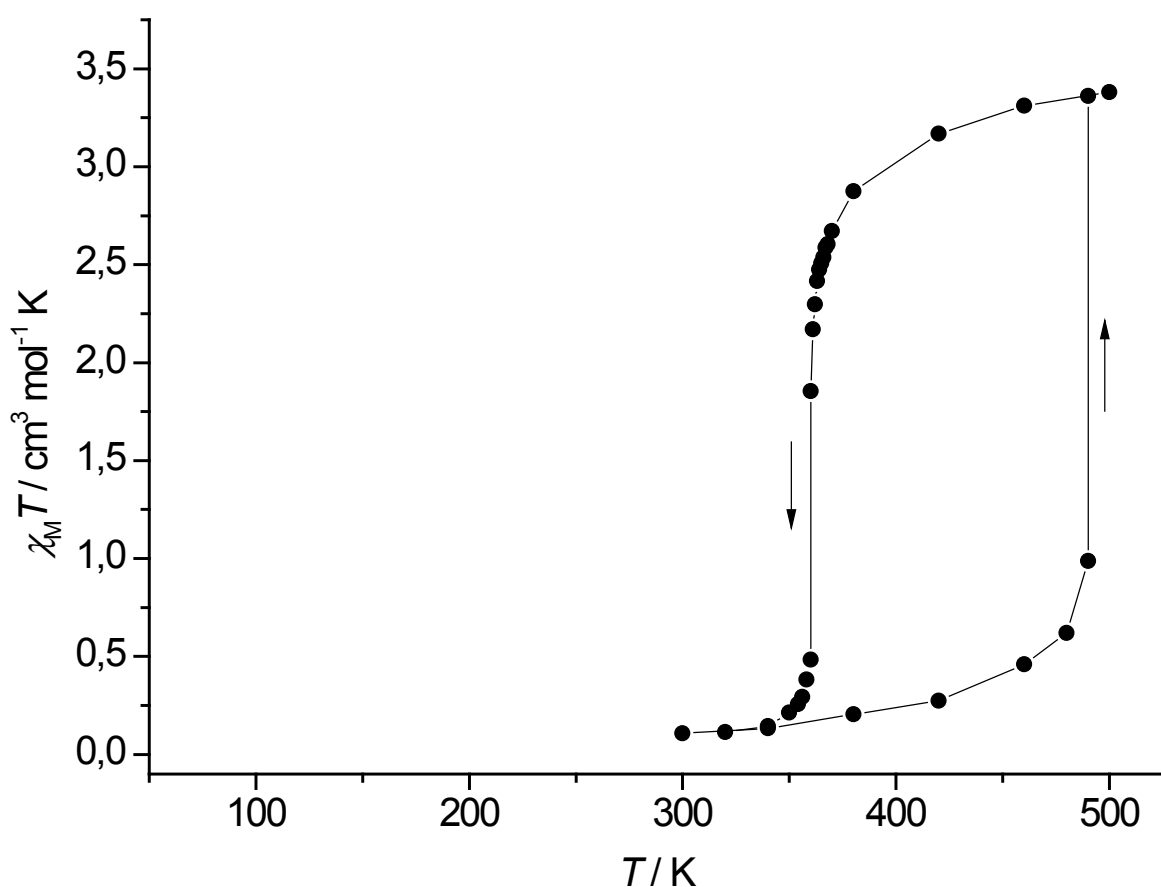


**Fig. S7** Thermal variation of  $\chi_M T$  for the spin transition  $\mathbf{1}^{\text{A/LS}} \leftrightarrow \mathbf{1}^{\text{A/HS}}$ .

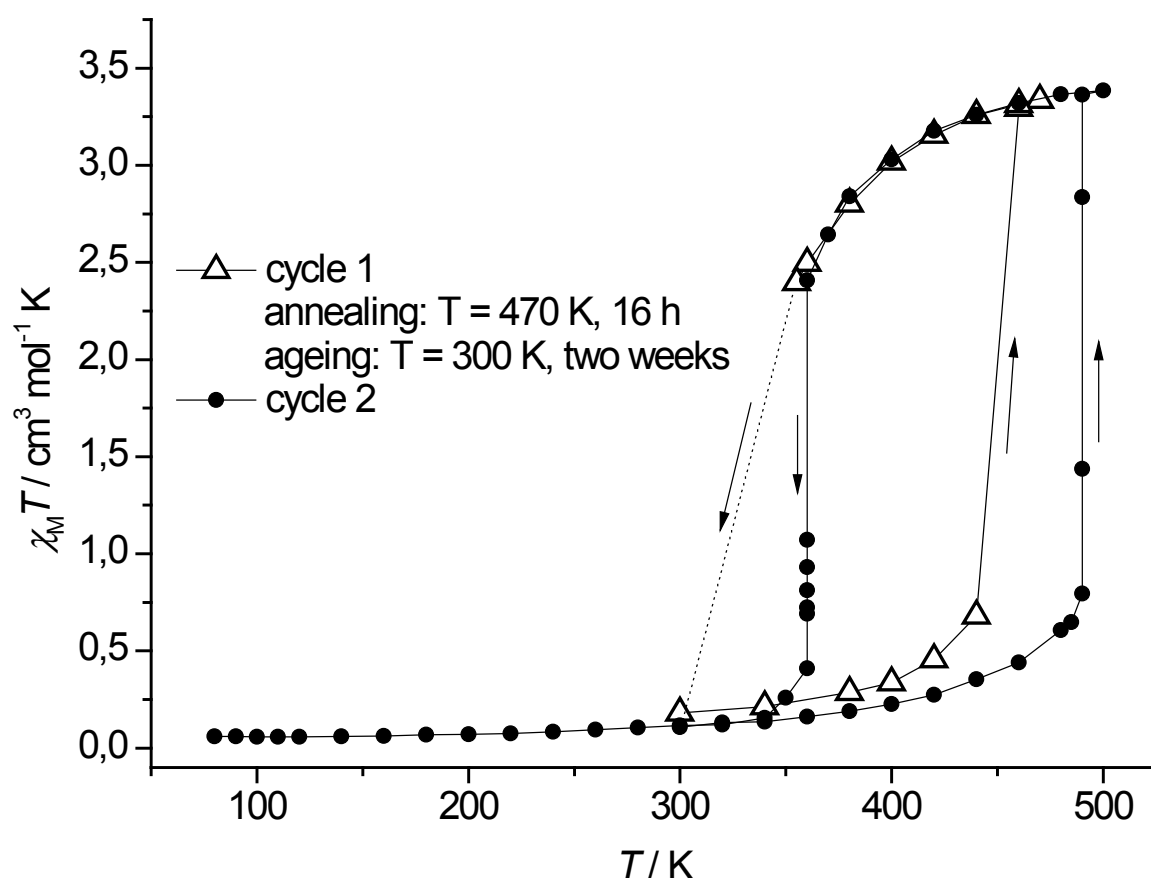


**Fig. S8** Thermal variation of  $\chi_M T$  for  $\mathbf{1}^{\text{LS}} \cdot x\text{H}_2\text{O}$ .

For the transition  $\mathbf{1}^{\text{A/LS}} \leftrightarrow \mathbf{1}^{\text{A/HS}}$  see cycle 2.

cycle 1:  $300 - 470\text{ K}$  (annealing, 16 h) –  $355\text{ K}$

$300\text{ K}$ , ageing for two weeks

cycle 2:  $300 - 500 - 80\text{ K}$

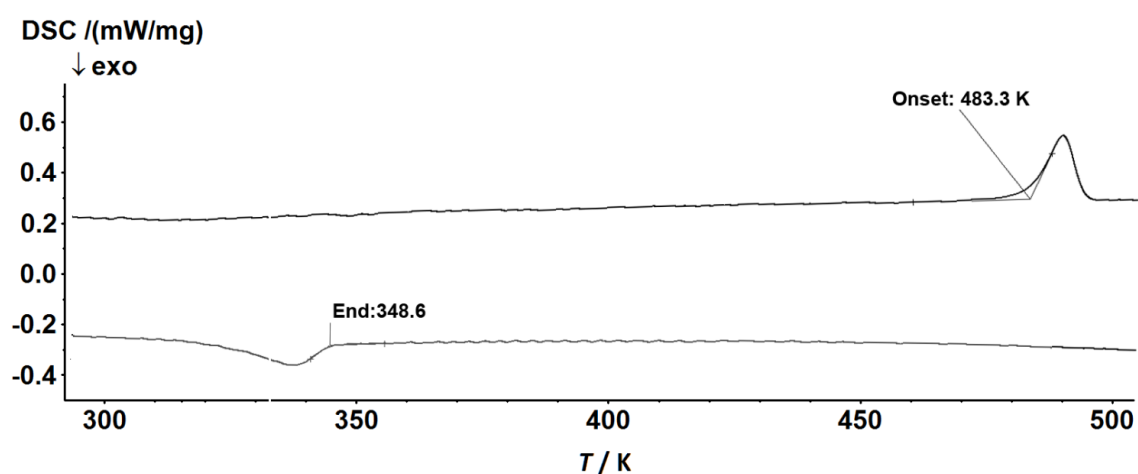


**Fig. S9** DSC curve for the transition  $\mathbf{1}^{\text{A/LS}} \leftrightarrow \mathbf{1}^{\text{A/HS}}$ .

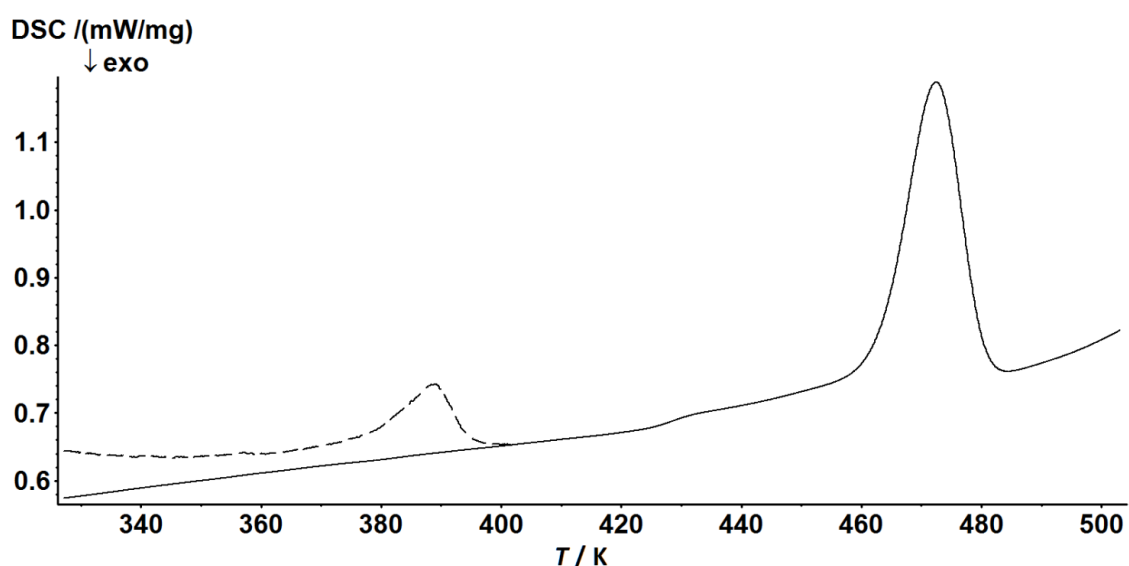


**Fig. S10** DSC curve for the transformation  $\mathbf{1}^{\text{LS}} \cdot x\text{H}_2\text{O} \rightarrow \mathbf{1}^{\text{B/HS}}$ .

First heating run: dashed line

Second heating run: solid line

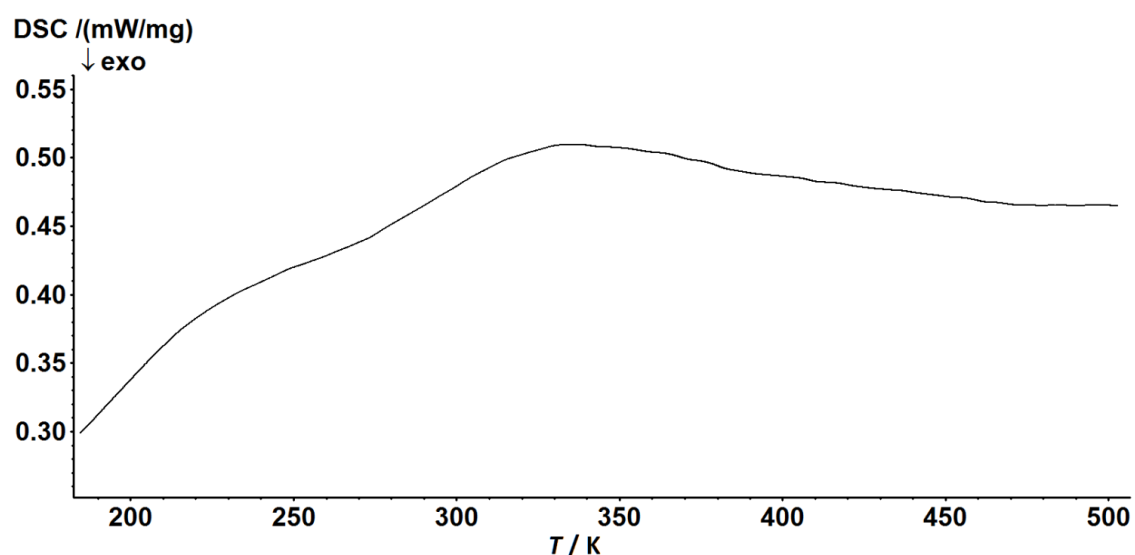


**Fig. S11** DSC curve for the transition  $\mathbf{1}^{\text{B/LS}} \rightarrow \mathbf{1}^{\text{B/HS}}$ .

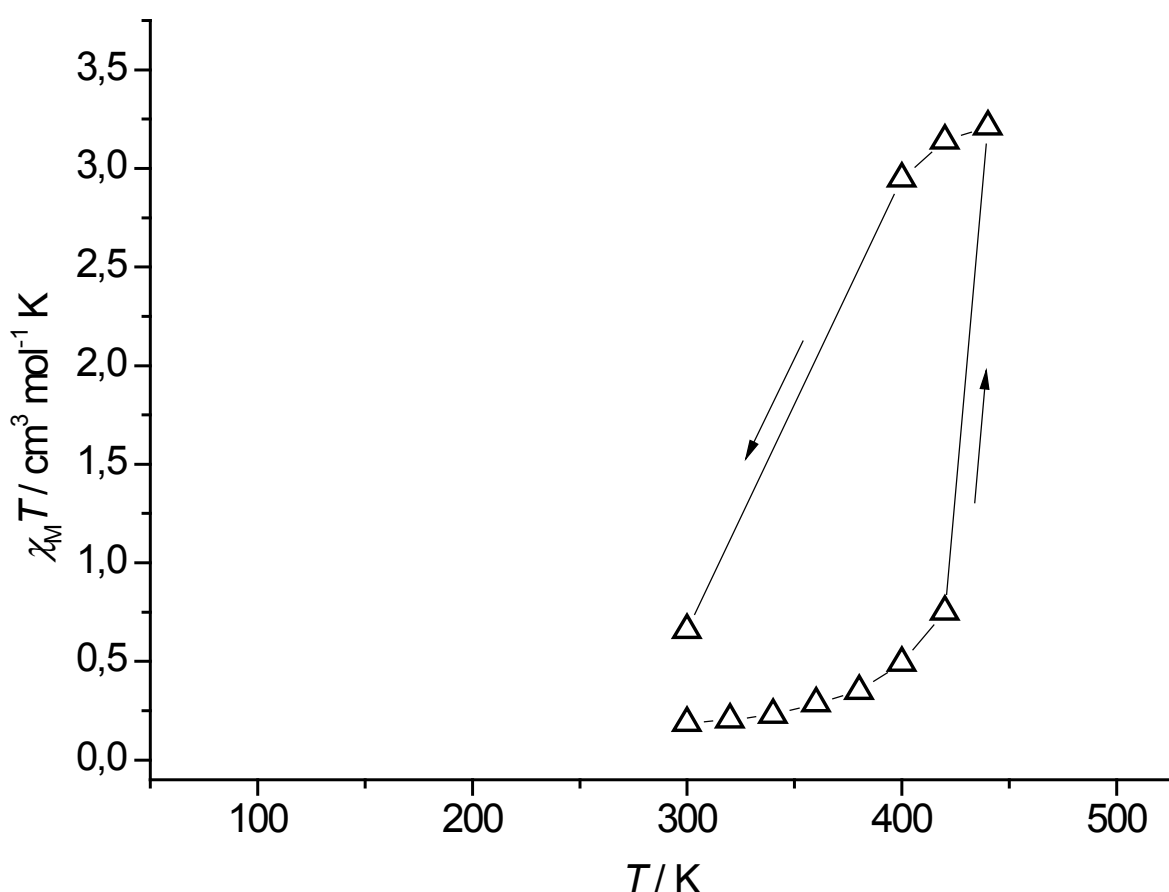


**Fig. S12** Thermal variation of  $\chi_M T$  for  $\mathbf{1}^{\text{LS}} \cdot x\text{H}_2\text{O}$  (first heating run).

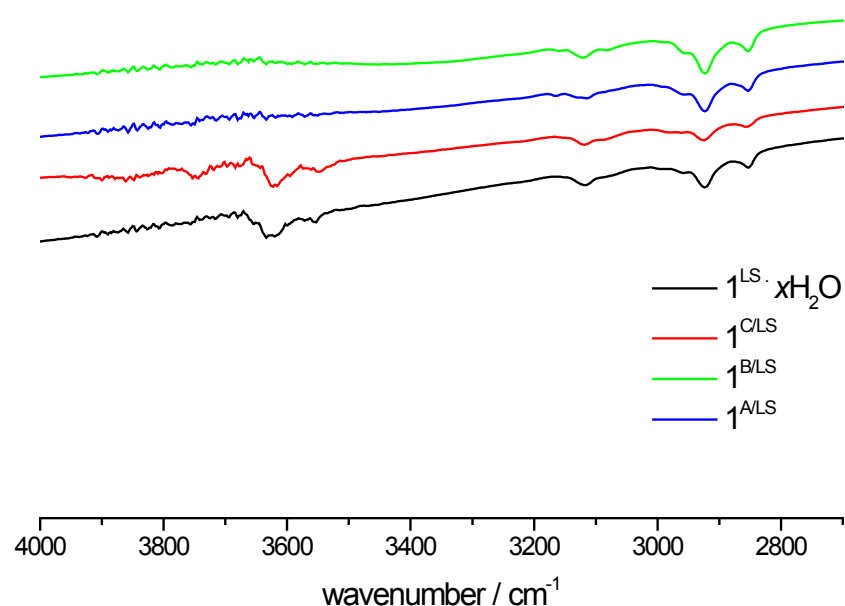


**Fig S13** IR spectra of  $1^{\text{LS}} \cdot x\text{H}_2\text{O}$ ,  $1^{\text{A}/\text{LS}}$ ,  $1^{\text{B}/\text{LS}}$  and  $1^{\text{C}/\text{LS}}$  (4000 – 2700 cm<sup>-1</sup>, fluorinated oil).

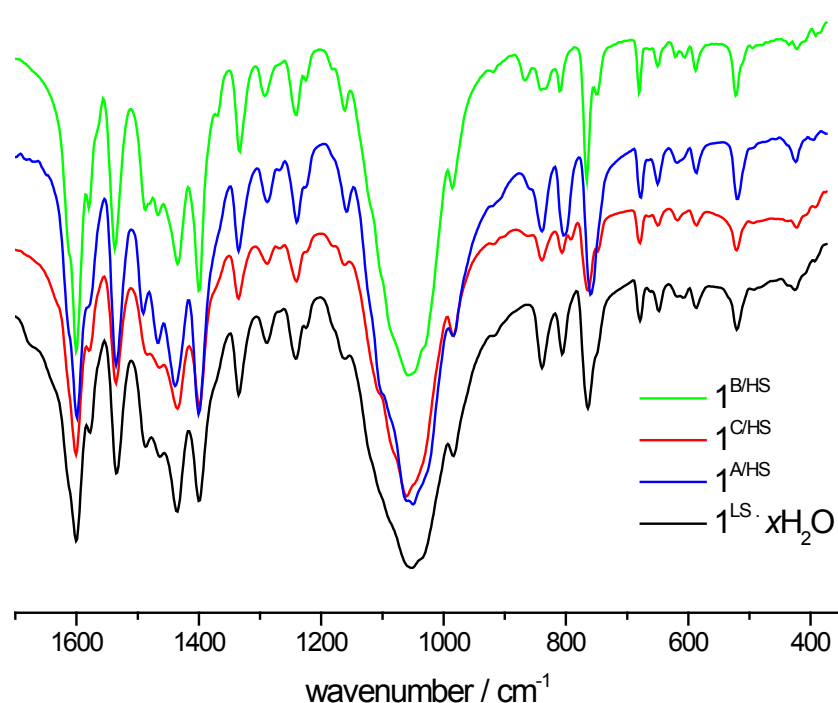


**Fig S14** IR spectra of  $1^{\text{LS}} \cdot x\text{H}_2\text{O}$ ,  $1^{\text{A}/\text{LS}}$ ,  $1^{\text{B}/\text{LS}}$  and  $1^{\text{C}/\text{LS}}$  (1700 – 350 cm<sup>-1</sup>, KBr).

The spectra of the phases are similar. The vibrations  $\nu_3(\text{B}-\text{F})$  and  $\nu_4(\text{B}-\text{F})$  are indicative of the outer-spheric nature of  $\text{BF}_4^-$ .

## Sorption/desorption of water in sealed ampoules

We estimated the possibility of reversible water sorption/desorption in the sealed ampoules. Thermal dependencies of water vapor pressure in the ampoule, saturated water vapor pressure and overall pressure in the ampoule are depicted in Fig S15 (ampoule volume is 150  $\mu\text{l}$ , sample weight is 2 mg,  $\mathbf{1}^{\text{LS}} \cdot \mathbf{xH}_2\mathbf{O}$ ,  $x = 0.5$ ). These results mean that the temperature-dependent sorption/desorption process is possible. For the system in equilibrium, in the region AB (Fig S15), partial pressure of water vapor in the ampoule is determined by saturated water vapor pressure while at higher temperatures (region BC) all water molecules should be in gaseous state. Thus, it seems reasonable that the first transformation of the parent complex  $\mathbf{1}^{\text{LS}} \cdot \mathbf{xH}_2\mathbf{O}$  into a mixture of two HS phases,  $\mathbf{1}^{\text{A/HS}}$  and  $\mathbf{1}^{\text{C/HS}}$ , is associated with dehydration. Annealing the parent complex at 370 K and 500 K in sealed ampoules also leads to dehydration.

On cooling, temperature-dependent condensation starts at *ca.* 340 K. This temperature is close to the temperature of the transition  $\mathbf{1}^{\text{A/HS}} \rightarrow \mathbf{1}^{\text{A/LS}}$  (360 K)<sup>†</sup>. However, among the three phases,  $\mathbf{1}^{\text{A/LS}}$ ,  $\mathbf{1}^{\text{A/HS}}$  and  $\mathbf{1}^{\text{C/HS}}$ , only the latter shows the tendency to absorb water (Fig S13) but it undergoes gradual spin crossover. This allows us to suppose that, in the case of the phases  $\mathbf{1}^{\text{A/LS}}$  and  $\mathbf{1}^{\text{B/LS}}$ , water molecules are predominately adsorbed on the ampoule walls and on the sample surface without entering the bulk phase. This suggests that reversible water release and uptake is probably not responsible for the abrupt spin state switching  $\mathbf{1}^{\text{A/LS}} \leftrightarrow \mathbf{1}^{\text{A/HS}}$ .

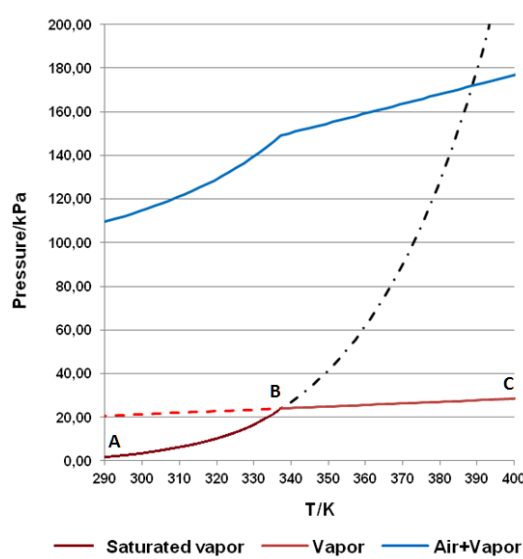


**Fig S15** Thermal dependencies of water vapor pressure, saturated water vapor pressure and overall pressure in the ampoule.

<sup>†</sup> Even if we suppose that condensation starts at 360 K, this means only that, for this temperature, partial pressure of water vapor is equal to the pressure of saturated water vapor. Thus, it seems unlikely that the beginning of water sorption abruptly switches the system from the HS state into the LS state. In addition, on lowering  $T$ , water can be adsorbed not only by the complex, but also by the ampoule walls.